Metasurfaces integrated with a single-mode waveguide array for off-chip wavefront shaping

SIYU CHEN,[1] JIANZHI HUANG,[1] SHENGQI YIN,[1] MILAN M. MILOSEVIC,[2] HAILONG PI,[1] JIZE YAN,[1] HAROLD M. H. CHONG[1] AND XU FANG[1,*]

[1]*School of Electronics and Computer Science, University of Southampton, Southampton SO17 1BJ, UK*
[2]*Zepler Institute for Photonics and Nanoelectronics, University of Southampton, Southampton SO17 1BJ, UK*
**x.fang@soton.ac.uk*

Abstract: Integration of metasurfaces and SOI (silicon-on-insulator) chips can leverage the advantages of both metamaterials and silicon photonics, enabling novel light shaping functionalities in planar, compact devices that are compatible with CMOS (complementary metal-oxide-semiconductor) production. To facilitate light extraction from a two-dimensional metasurface vertically into free space, the established approach is to use a wide waveguide. However, the multi-modal feature of such wide waveguides can render the device vulnerable to mode distortion. Here, we propose a different approach, where an array of narrow, single-mode waveguides is used instead of a wide, multi-mode waveguide. This approach tolerates nano-scatterers with a relatively high scattering efficiency, for example Si nanopillars that are in direct contact with the waveguides. Two example devices are designed and numerically studied as demonstrations: the first being a beam deflector that deflects light into the same direction regardless of the direction of input light, and the second being a light-focusing metalens. This work shows a straightforward approach of metasurface-SOI chip integration, which could be useful for emerging applications such as metalens arrays and neural probes that require off-chip light shaping from relatively small metasurfaces.

1. Introduction

Metasurface, an ultrathin layer of judiciously designed artificial micro- and nano-structures, has shown extraordinary capabilities in manipulating electromagnetic waves [1]. These capabilities are widely explored in the form of wavefront shaping in free space, where a free-space optical mode (usually a single or multiple freely propagating plane waves) is converted to another free-space mode (e.g. an optical vortex [2], a hologram [3], a focus [4] or a deflected light beam [5]). Similarly, metasurfaces can also realize conversion between different confined optical modes, to facilitate functionalities such as asymmetric power flow [6], light focusing [7, 8], mode conversion [9], signal routing [10] and fiber-to-chip coupling [11]. In these two categories of metasurfaces, the input and output can be considered as belonging to the same group of light: they are either both free-space light or both guided light. Whereas, this work targets a third category of metasurfaces, where they bridge these two groups and allow for the transition between various free-space modes and guided modes [12]. Metasurfaces in this category can leverage advantages of integrated devices (e.g. a small form factor and a high integration density) while providing optical access to free space. In particular, in the form of meta-structured waveguides, or meta-waveguides [12], they could lead to novelty solutions for emerging applications such as augmented reality projection [13, 14], LiDAR (light detection and ranging) [15] and free-space optical communication [16].

Being a versatile tool for wavefront shaping, metasurfaces can transit an incident free-space light beam into a range of different guided modes, including surface plasmons on a metal film

[17-19], driven surface waves on a dielectric meta-grating [20], whispering gallery modes in a microcavity [21], as well as waveguide modes in straight waveguides [22, 23]. The transition can also be in the opposite direction: for example, for input as a waveguide mode on a photonic chip, the corresponding output is off chip in free space. Functionalities such as light focusing [24-27], beam deflection [28], optical vortex generation [29, 30], holography [31-34] and Airy beam generation [35] have all be realized by decorating waveguides with metasurfaces.

Aiming at future applications utilizing the photonic integrated circuit platform, this work concentrates on using integrated metasurfaces to extract light from Si waveguides on an SOI (silicon-on-insulator) chip. To enable off-chip wavefront control in all the three dimensions above a waveguide, the metasurface has to be a 2D (two-dimensional) array of light scatterers, as opposed to a single line of light scatterers on top of a stand-alone waveguide [12]. To optically drive such 2D arrays, the existing solution is to use a wide waveguide [12]. However, a wide waveguide usually supports multiple eigen modes, and the integrity of the input mode is consequently vulnerable to perturbations to the driving field (see Section A of the Supplementary Information for a numerical demonstration). This solution thus requires all the light scatterers to be extremely weak in strength, which increases not only the complexity of the nanostructures but also the challenges in device design and nanofabrication. In this work, we show an alternative approach to integrate a 2D metasurface with waveguides: to use an array of single-mode waveguides. This integration has a relatively straightforward device layout and is suitable for off-chip light shaping applications that only require a limited aperture.

2. Generic device structure and the 2π phase coverage

Figure 1(a) shows schematically the generic layout of the proposed all-dielectric, waveguide-driven metasurfaces. The layout shares a key feature with the conventional metasurfaces that bridge two free-space modes: it contains a planar, subwavelength array of light scattering units. The major difference here is that, all the units now reside on top of light-feeding Si waveguides. For a conventional metasurface illuminated by a plane wave, all the light scatterers are assumed to be driven at the same strength and the same phase by the incident light, and this assumption has been a fundamental principle for metasurface design. For the layout shown in Fig. 1(a), the incident light inevitably changes its phase and strength as it propagates along the waveguides, clearly violating this design principle. Consequently, the traditional design strategies have to be modified for the integrated metasurfaces discussed here.

A new design method can be obtained by examining an individual metasurface element shown in Fig. 1(b). The element here, named as an MBB (Meta-waveguide Building Block), consists of a light emitting Si cylinder and a section of light-feeding Si waveguide of length p. Light emitted by an MBB thus has a phase of θ that contains two parts

$$\theta = \theta_c + \theta_w \tag{1}$$

where θ_c and θ_w are the contribution of the vertical cylinder and the horizontal waveguide, respectively. To simplify the design process, we have chosen to restrict the freedom of θ_w in Eq. (1). The map on the left of Fig. 1(c) shows a hypothetical target phase profile for a functional metasurface, a key feature of which is the continuous phase variation across the whole map. This phase profile is sampled at a periodic interval for element selection, as seen on the right of the figure. By restricting p, which is equivalent to the sampling periodicity along the light propagation direction, it is possible to reduce θ_w to a constant for all the MBBs, regardless of their ultimate positions in a metasurface. Here, we set p as

$$p = \lambda_{eff,w} = \lambda_0/n_{eff,w} \tag{2}$$

where $\lambda_{eff,w}$ is the effective wavelength of the input light inside the waveguide (i.e. the distance over which the optical phase goes over a 2π cycle), λ_0 is the wavelength in free space, and $n_{eff,w}$ is the associated effective refractive index. Equation (2) also implies that $n_{eff,w}$ is the spatial sampling rate of the output wavefront with respect to λ_0 along the waveguide direction [Fig. 1(c)]. It is worth noting that, the constraint of Eq. (2) does not apply to the MBB

periodicity in the orthogonal planar direction, due to the lack of θ_w (i.e. propagation) in this direction.

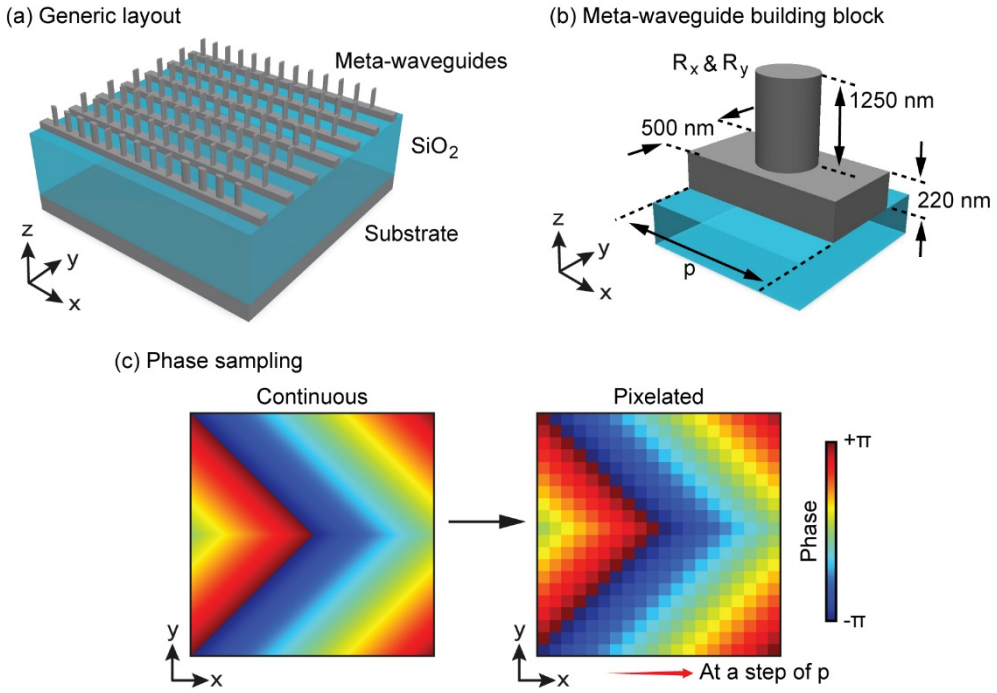

Fig. 1. Schematic of a generic design of a Si waveguide-integrated metasurface. (a) The device utilizes the widely adopted SOI (silicon-on-insulator) platform. The waveguides in the *xy* plane feed energy to the light scatterers, which are *z*-oriented Si nanopillars arranged in a planar array. (b) The smallest unit of the device is a meta-waveguide building block (MBB). It consists of a section of waveguide that is 220 nm in height, 500 nm in width, and p in length. On top of the center of the waveguide is a Si nanopillar. Its height along the z axis is 1250 nm. It has an elliptical cross section, with the dimensions R_x and R_y as tunable parameters. The Si substrate visible in panel (a) is not depicted here, in order to improve visualization. (c) A target output wavefront, where the phase changes continuously with position, is approximated pixel by pixel in the integrated metasurface. To simplify the design process, the waveguide length p is set to be identical or very close to $\lambda_{eff,w}$, the effective wavelength in the waveguide.

The numerical simulation was conducted using FDTD (finite-difference time-domain) method-based commercial software (Lumerical). The SiO_2 BOX (buried oxide) layer of the SOI (silicon-on-insulator) wafer had a thickness of 2 μm, optically isolating the waveguide from the bottom Si substrate. The refractive indices [36] of the Si and SiO_2 were set as 3.48 and 1.44, respectively, at λ_0 of 1550 nm. The Si waveguide was 220 nm in height and 500 nm in width, and it supported only a single TE mode. For an isolated (i.e. far away from any adjacent waveguide), bare (i.e. having no nanopillar on top) waveguide, $\lambda_{eff,w}$ was found to be 650.2 nm, corresponding to an effective index $n_{eff,w}$ of 2.384. In a metasurface-decorated waveguide array, $\lambda_{eff,w}$ is affected by both the nano-scatterers and inter-waveguide coupling (see Section B in the Supplementary Information for details). As discussed in more details in Sections 3 and 4, $\lambda_{eff,w}$ is approximately 625 nm and 630 nm in the beam deflector and the metalens, respectively.

Figure 2 shows the dependence of θ_c, the contribution to output phase from Si cylinders, on the cylinder's cross section. The simulation is conducted on a single waveguide surrounded by perfectly matched layers, and input light is fed into the waveguide beneath the nanopillar. All the cylinders have a uniform height of 1250 nm and an elliptical, but tunable, cross section.

One of the principal axes of the ellipse is always aligned along the waveguide (i.e. the *x* axis in Fig. 1), with the light experiencing a right-left mirror symmetry as it propagates forward in the waveguide. This right-left mirror symmetry forbids the *y*-polarized incident light from generating any *x*-polarized output, which eliminates polarization rotation in the output and simplifies analysis. Parametric sweep is conducted by tuning the principal semi-axis dimensions R_x and R_y from 70 nm to 250 nm at a step of 10 nm, with the upper boundary of 250 nm constrained by the width of the waveguide. This sweep creates a library of $19 \times 19 = 361$ nanopillar geometries that is analyzed in Fig. 2.

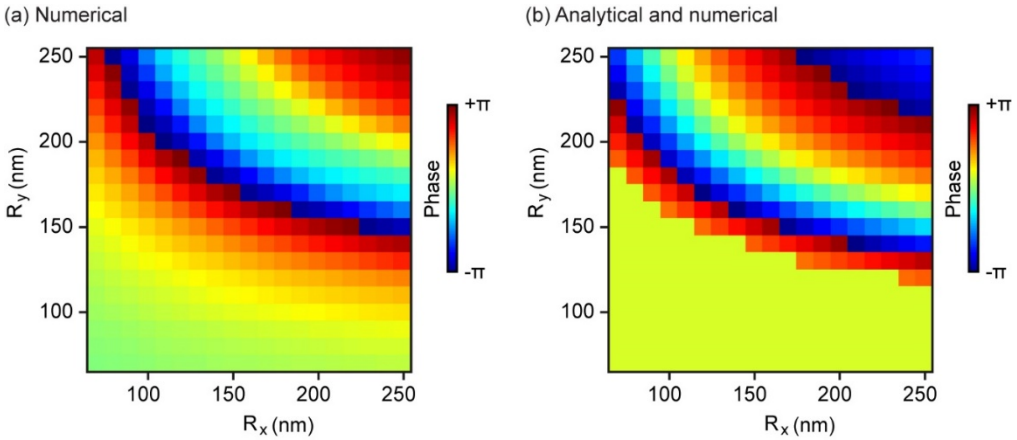

Fig. 2. Output phase of nanopillars, obtained from (a) numerical simulation and (b) a numerical-analytical hybrid approach. The principal semi-axis dimensions R_x and R_y range from 70 nm to 250 nm at a step of 10 nm. The values in both maps are normalized against the phase of the smallest nanopillar, which has $R_x = R_y = 70$ nm.

Figure 2(a) shows the numerically simulated output phase of these 361 nanopillars, all extracted from the same location that is 2 μm above the nanopillar top. The values shown here have been normalized against the value of the smallest nanopillar (i.e. $R_x = R_y = 70$ nm), a process that eliminates the contribution of θ_w for any value of p. As this smallest, reference nanopillar well approximates a point scatterer, the phase shown in Fig. 2(a) can be interpreted as the output phase of nanopillars θ_c, normalized against an infinitesimally small, point scatterer.

The phase distribution shown in Fig. 2(a) consists of multiple curved bands that are roughly symmetric with respect to the diagonal line that connects the smallest ($R_x = R_y = 70$ nm) to the largest nanopillar ($R_x = R_y = 250$ nm). This symmetry suggests that R_x and R_y have roughly equal influence on the output phase. This conclusion, combined with the shape of the bands, further indicates that θ_c mostly depends on the cross-sectional area of these nanopillars. Nevertheless, θ_c still shows a different sensitivity to R_x and R_y in Fig. 2(a). This is because the input electric field beneath the nanopillar is dominantly *y*-polarized.

A critical feature of Fig. 2(a) is the full 2π phase coverage, which suggests the possibility of full wavefront control in such waveguide-driven metasurfaces. Regarding the origin of this phase coverage, the tall (height at 1250 m) and thin (R_x and R_y equal 250 nm at maximum) shape of the nanopillars suggests that it comes from light propagation. To verify this assumption, a propagation phase is calculated for each nanopillar and shown in Fig. 2(b). This propagation phase is expressed as $2\,\pi\,h/\lambda_{eff,c}$, where h is the height of the cylinder and equals 1250 nm. Meanwhile, $\lambda_{eff,c}$ is the effective wavelength of light inside each type of cylinder, obtained in numerical simulation by assuming an infinite cylinder height. The value of $\lambda_{eff,c}$ depends on the cross-sectional size and shape of the cylinder, and reaches the smallest value of 563.8 nm in the largest nanopillar (i.e. $R_x = R_y = 250$ nm). For small nanopillars (with $R_x \times$

R_y roughly below 150 × 150 nm^2), no guided mode exists, and the value of $\lambda_{eff,c}$ thus takes 1550 nm in the calculation. This method is a numerical-analytical hybrid method [37], as it contains both a numerical element (in the calculation of $\lambda_{eff,c}$) and an analytical element (in the assumption of the dominance of the propagation phase). Although different in the absolute values for many nanopillars, the phase map computed using this method [Fig. 2(b)] possesses a high degree of similarity to the purely numerical results [Fig. 2(a)], in both the overall phase coverage and the dependence on planar dimensions. This similarity confirms that the 2π phase coverage in Fig. 2(a) mainly comes from the phase accumulation in light propagation, which is either mostly in free space (for small pillars) or as a guided mode (for larger pillars).

To demonstrate the light manipulation capability promised by the 2π phase coverage, we have designed and evaluated two types of functional metasurfaces, one as a beam deflector and the other a light-focusing lens. They are discussed in the following two sections separately.

3. Metasurface beam deflector as the first example device

The metasurface beam deflector discussed in this section (Fig. 3) possesses a unique light-manipulation capability: it emits light into the same direction, even if the input light reverses its direction. In other words, it has a constant *absolute* light deflection angle. This is in sharp contrast to a conventional grating, where it is the *relative* light deflection angle that stays invariant with changing the input direction. To be more specific, the *absolute* deflection angle is the angle between the light emission direction and a fixed coordinate, and it is defined here as the deviation from the +*z* direction (i.e. the vertical direction) towards the +*x* direction. By comparison, the *relative* deflection angle is with respect to the variable incident light direction.

To reveal the contrast between the meta-deflector and a conventional grating in light emission, we first derive a generic light deflection equation that encompasses both types of devices. Here we consider an array of Si waveguides in the *xy* plane on top of a BOX layer, which has the same layout as shown in Fig. 3(a). All the waveguides are along the *x* axis, and they are evenly spaced along the *y* axis at a subwavelength interval. On each waveguide, a line of light scatterers is evenly spaced at a periodicity of p (it can take any subwavelength value at this stage of general analysis), which may possess a phase gradient of k_p along the +*x* direction in light scattering. For light deflection in the *xz* plane, the deflection angle can be obtained by matching the in-plane momentum between the guided mode and the output light. The *absolute* deflection angle α is derived to be

$$\alpha = \arcsin\left[\lambda_0\left(\pm\frac{1}{\lambda_{eff,w}} + n\frac{1}{p} + \frac{k_p}{2\pi}\right)\right] \tag{3}$$

where the sign before the term $1/\lambda_{eff,w}$ is determined by the direction of the input light, and n is an integer that describes the diffraction order. Note that all the three terms in the parenthesis do have the same unit of inverse meter.

A clear difference exists between the two terms of $1/\lambda_{eff,w}$ and $k_p/2\pi$ in Eq. (3): the former depends on the input direction while the latter does not. If all the light scatterers are identical, as in a conventional waveguide-integrated grating, we have $k_p = 0$. If this grating only has a single deflection order, with $n = 1$ or $n = -1$, the angle α then switches between $\arcsin(\lambda_0/\lambda_{eff,w} - \lambda_0/p)$ and $-\arcsin(\lambda_0/\lambda_{eff,w} - \lambda_0/p)$ with reversing the direction of input light. In comparison, for the beam deflector in Fig. 3, as $p = \lambda_{eff,w}$ and $k_p \neq 0$, we can reduce Eq. (3) to

$$\alpha = \arcsin(\lambda_0\, k_p/2\pi) \tag{4}$$

for both input directions, with n chosen suitably. This solution implies that, in such meta-deflectors, the absolute output angle can indeed stay unchanged.

In the example metasurface shown in Fig. 3, four different MBBs are selected from the library in Fig. 2 to form a metasurface super unit cell (see Section C of the Supplementary Information for the dimensions of each nanopillar), and the super unit cell is repeated by six times along a waveguide. As mentioned in Section 2, the value of p follows that of $\lambda_{eff,w}$, and

it is set as 625 nm here. Figure 3(b) shows that these 24 MBBs produce a linear phase ramp that changes by $\pi/2$ over every 625 nm along a waveguide. The whole metasurface contains 12 identical waveguides placed at a periodicity of $2p = 1250$ nm along the *y* axis. A value of 1250 nm rather than 625 nm is chosen here, as it can reduce inter-waveguide coupling and side leakage [38-40] and the nanopillar array still remains in the subwavelength regime. For all the 12 waveguides, the input is assumed to be uniform in phase and intensity, which can be realized in experiment by using a multi-stage binary splitter tree [41, 42].

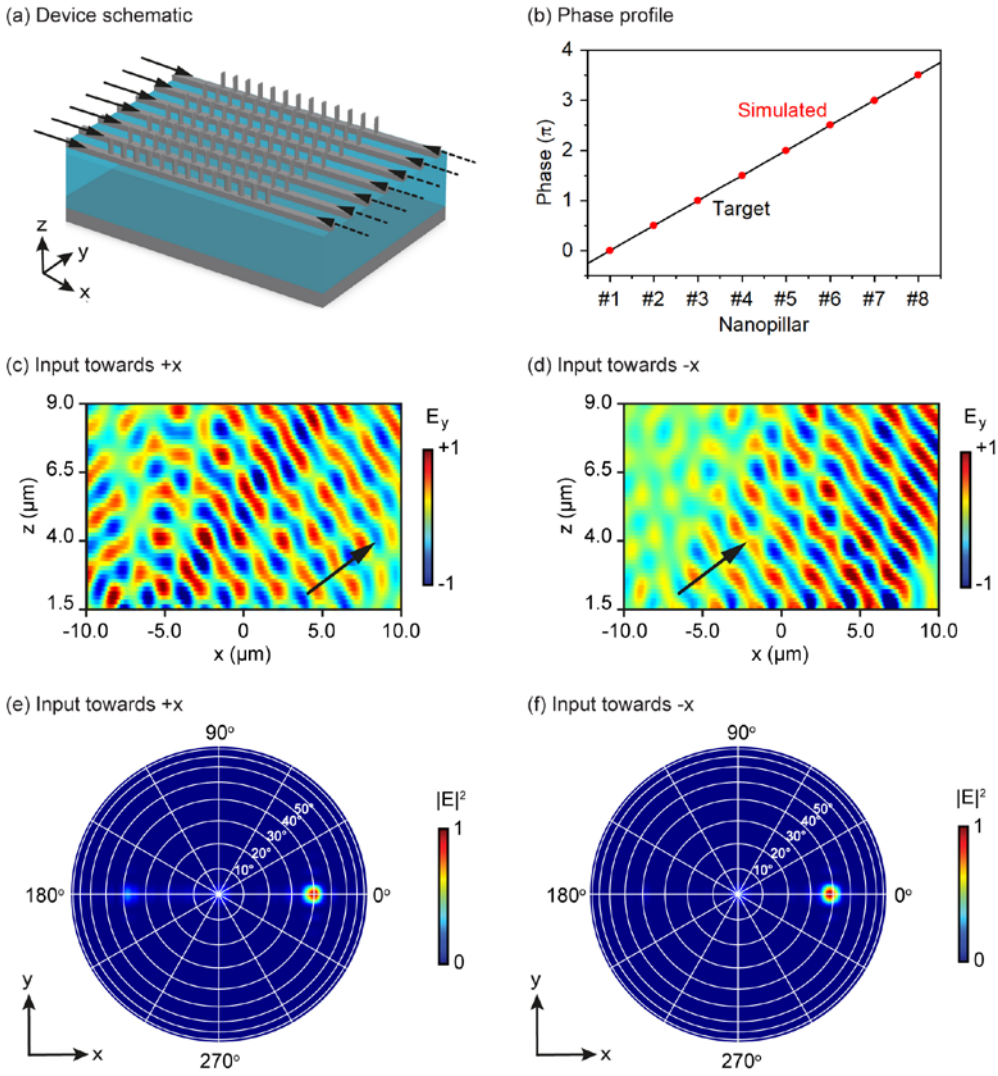

Fig. 3. The first example design: a metasurface beam deflector. (a) Schematic of the meta-deflector. The simulated device contains 12 identical waveguides, with 24 nanopillars on top of each waveguide. The input light is along either the +*x* direction (the solid arrows) or the -*x* direction (the dashed arrows). (b) Output phase profile θ_c along a section of a waveguide, with the theoretical target (the black line) compared against the numerical output (the red dots). (c) Output electric field in an area of 20 μm × 7.5 μm at the central *xz* plane of the metasurface. The bottom of the area is 1.5 μm above the top of the nanopillars. The field is normalized against its peak amplitude in the map. The input light propagates in the +*x* direction. The direction of the main output is indicated using the black arrow. (d) The corresponding electric field in the same area, with the input light reversed in its direction. (e, f) Electromagnetic intensity distribution in the far field. The input light propagates along (e) the +*x* direction and (f) the -*x* direction.

The phase ramp seen in Fig. 3(b) is intrinsic to the nanostructure design and does not change with the direction of the incident light. This feature is clearly observed in the near-field light scattering from the nanopillars [Figs. 3(c) and 3(d)], where the majority of the output propagates towards the top-right corner in both maps. Differences in the details between the two maps are mainly attributed to the shadowing effect, for which nanopillars closer to the light source experience stronger excitation. The influence of this effect appears to be more pronounced in Fig. 3(c) than in Fig. 3(d), in the form of stray output towards the top-left corner of the map. This phenomenon is further discussed at the end of Section 4.

As compared to the near-field maps of Figs. 3(c) and 3(d), the far-field distributions show even weaker dependence on incident direction [Figs. 3(e) and 3(f)]. For input towards the $+x$ direction, the output peaks at 39.7°, with an FWHM (full width at half maximum) along the x axis at 8.5° [Fig. 3(e)]. For the $-x$ input, the output peaks at a very similar angle of 38.0°, and the x-axis FWHM is 8.9° [Fig. 3(f)]. These two deflection angles, 39.7°and 38.0°, are very close to the theoretical value derived from Eq. (3), which is 38.3°. The very small difference in the deflection angle between the two input directions can be eliminated by slightly tuning the input wavelength (see Section D in the Supplementary Information for details). The effective aperture along the x axis, which can be derived from the FWHM, is about 12 μm, or 80% of the physical aperture. It indicates that light has decayed significantly as it reaches the end of the metasurface. The output efficiency, defined as the power ratio of the main output beam [extracted from the far fields shown in Figs. 3(e) and 3(f)] and the total input, is 11.7% and 28.7% for the $+x$ and the $-x$ input direction, respectively. The lower efficiency in Fig. 3(e) can be associated with the stronger stray light seen in Fig. 3(c), which in turn is attributed to a stronger shadowing effect. To make the diffraction efficiency less sensitive to input direction, a potential solution is to include the scattering efficiency of each nanopillar into element selection.

4. Metalens as the second example device

In this section, we use a metalens as the second example device (Fig. 4). Unlike the beam deflector shown in Section 3, where the phase gradient is only uniaxial, here the phase gradient is radial from the center of the nanopillar array, meaning that the nanopillars are no longer identical across waveguides. Here we consider a metalens that produces a spherical wavefront in free space, which requires a hyperbolic phase profile in the metasurface output [43]:

$$\theta_c = \frac{2\pi}{\lambda_0}\left(\sqrt{r^2 + f^2} - f\right) \tag{5}$$

where r is the radial distance from the center of the metalens, and $f = 50$ μm is the focal length.

Figure 4(a) shows the schematic of the device. Different from the previous device of beam deflector where all the waveguides have the same input, here the input light reverses its direction between adjacent waveguides. This change provides two benefits: it improves the symmetry of the output focus, and it increases the effective aperture of the device. The second feature will be discussed in more details at the end of this section. The whole device contains 45 (the number of waveguides) × 45 (the number of nanopillars on top of each waveguide) nanopillars, distributed in a square array with a lattice constant of 630 nm along both the x and the y axes. The dimensions of 23 representative nanopillars are listed in Section C of the Supplementary Information. Figure 4(b) shows the output phase of all the 2025 nanopillars in this device. The maximal phase coverage, which is from a corner to the center of the map, is $2.6 \times 2\pi$. The derivation from the target phase averages at 1.9°, which is a very small value. This excellent phase match can be visualized in Fig. 4(c), which compares the simulated output of 45 nanopillars [taken along the line of $y = 0$ in Fig. 4(b)] against the analytical target of Eq. (5).

Figures 4(d), 4(e) and 4(f) show the output focus at the xz, yz and xy plane, respectively. A clear and well-defined focus is observed. The focal length, defined as the distance between the nanopillar top plane and the location with the highest field intensity, is 46.5 μm, slightly shorter

than the target value of 50 μm. The FWHM of the focus is 2.41 μm, approximately 1.55 λ_0, along the central *x* axis. Meanwhile, it is 2.59 μm, approximately 1.67 λ_0, along the central *y* axis. The output efficiency, with the output power computed in a square of 7.77 μm × 7.77 μm (three times of the FWHM along the *y* axis) at the focal plane, is 18.2%. Several weak, isolated sidebands are observed along the *x* and *y* axis across the center of the focus, which originate from the square shape of the lens. Here, we took the side length of the lens as $l = 27.72\ \mu m$ (i.e. the distance between the centers of the outmost nanopillars along the *x* and *y* axis), and calculated the Fraunhofer diffraction pattern at the focus. The theoretical results, obtained from $sinc^2[\pi\ l\ x/(f\ \lambda_0)]$ and $sinc^2[\pi\ l\ y/(f\ \lambda_0)]$, match well with the simulated intensity in Figs. 4(g) and 4(h). This close match confirms the high quality of the light focusing; it also confirms that the effective aperture reaches the value of the physical aperture.

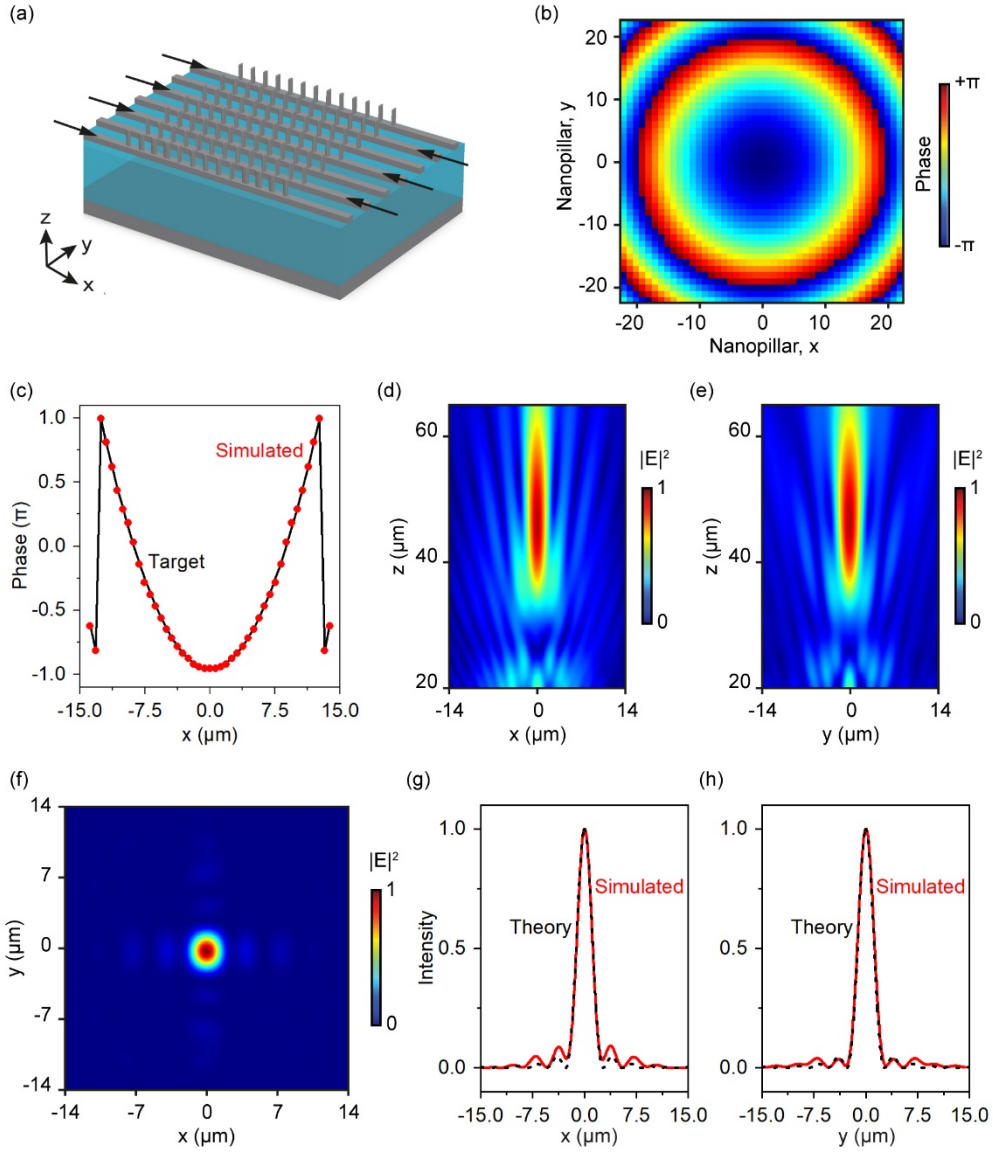

Fig. 4. The second example design: a light-focusing metalens. (a) Schematic of the device. The simulated device contains 45 × 45 nanopillars, and the input light reverses its direction (the black arrows) between adjacent waveguides. (b) The output phase profile θ_c of all the 2025

nanopillars. After all the nanopillars are selected and assembled here, their phases are adjusted by a constant to set the phase at the center of the map to -π. This adjustment is purely for visualization and does not affect the overall phase coverage of the map. (c) The simulated output phase of the nanopillars along the central waveguide (the red dots), compared against the analytical target phase profile (the black line). (d-f) Electromagnetic field intensity of the focus, shown in (d) the *xz* plane, (e) the *yz* plane, and (f) the *xy* plane. (g, h) Field intensity along (g) the *x* axis and (h) the *y* axis across the center of the focal spot, with the numerically simulated results (the solid lines) compared against the analytical results (the dashed lines).

Before concluding this work, it is worth discussing more on the novelty of the waveguide array proposed in this work, after two example devices have been analyzed. The nanopillar selection used in both devices [Figs. 3(b) and 4(b)] is based on the assumption that the output phase of any individual nanopillar [Fig. 2(a)] is independent from its position in a metasurface. As shown in Fig. S1(b) in the Supplementary Information, this assumption becomes invalid in a wide, multi-mode waveguide, because the phase of input light beneath a nanopillar is noticeably affected by the presence of other nanopillars. In this case, each nanopillar will respond not only to the input light but also to light scattered by other nanopillars, similar to the meta-atoms in some light-emitting metasurfaces [44]. Moreover, as shown in the second device, the waveguide array brings another benefit, which is the separation of input light that propagates in oppose directions. If the metalens discussed in this section is integrated with a single wide waveguide instead, sending light into the waveguide in opposite directions would create a standing wave. Although a metalens can be driven by a standing wave of freely propagating light and show interest coherent tuning [45], it remains an open question whether the integrated version of such coherently controlled metalenses also exists.

It is also worth discussing some key differences between these meta-waveguides and the most investigated, free-space metasurfaces. Although for the latter, it is a common practice to assume that all the meta-atoms are driven at the same phase and the same strength by an input, this assumption has to be treated with more caution in the meta-waveguides discussed here. By setting the length of an MBB to a single effective wavelength, we have shown that, it is possible to drive all the meta-atoms at the same phase. Nevertheless, a shadowing effect still exists, where the Si nanopillars further down a waveguide are driven at weaker strength, as seen in Section A in the Supplementary Information. A clear sign of this shadowing effect is a smaller effective aperture as compared to the physical aperture, as seen in the first example device. Suppressing the scattering strength of individual meta-atoms could weaken this effect, but this approach necessitates designing more complicated meta-atoms and is beyond the scope of this proof-of-principle demonstration. As an alternative approach to partly circumvent this problem, the second example device alternates the input direction between adjacent waveguides. The effective aperture along the waveguide has doubled to ~28 μm, as compared to the first example device, and it equals the physical aperture.

5. Conclusion

To conclude, we have proposed and numerically tested a new design approach for SOI chip-integrated metasurfaces. In this new approach, the metasurface is integrated with an array of single-mode waveguides. As these waveguides only support the fundamental TE modes, the input mode is relatively robust against perturbation induced by nano-scatterers. As a result, Si nanopillars can be placed directly on top of these waveguides to produce the 2π phase coverage required for full wavefront shaping. Two example devices have been designed and numerically characterized. The first device, a metasurface beam deflector, can deflect light at the same absolute angle (approximately 38°) at both input directions. The second device, a metalens, can focus light at 46.5 μm above the metasurface, into a focal spot approximately the same size as the ideal Fraunhofer diffraction.

The off-chip light shaping capabilities demonstrated here could be useful for devices where a relatively small planar size (e.g. below 100 μm as side length) is desirable (e.g. in neuro probes [46-48]). The waveguides and the nanostructures of these devices are all made of Si

only, suggesting that they can be mass produced at low cost using standard CMOS fabrication technology [49]. Factors such as tolerance to potential pillar-waveguide misalignment and phase/power fluctuation across the input channels need be tested in future experiments. As each waveguide in the array could be addressed individually, this device configuration could be explored in the future to realize more advanced wavefront shaping and wavelength multiplexing [50] functionalities.

Funding. Royal Society (IEC\R3\183071, IES\R3\183086); Engineering and Physical Sciences Research Council (EP/V000624/1).

Disclosures. The authors declare no conflicts of interest.

Data availability. The data that supports the findings of this study are available within this article.

Supplemental document. See Supplement 1 for supporting content.

References

1. S. Sun, Q. He, J. Hao, S. Xiao, and L. Zhou, "Electromagnetic metasurfaces: physics and applications," Adv. Opt. Photonics. **11**(2), 380-479 (2019).
2. Y. Ming, Y. Intaravanne, H. Ahmed, M. Kenney, Y. Q. Lu, and X. Chen, "Creating Composite Vortex Beams with a Single Geometric Metasurface," Adv Mater **34**(18), 2109714 (2022).
3. J. Kim, D. K. Oh, H. Kim, G. Yoon, C. Jung, J. Kim, T. Badloe, H. Kang, S. Kim, Y. Yang, J. Lee, B. Ko, J. G. Ok, and J. Rho, "Metasurface Holography Reaching the Highest Efficiency Limit in the Visible via One-Step Nanoparticle-Embedded-Resin Printing," Laser Photonics Rev. **16**(8), 2200098 (2022).
4. F. He, Y. Feng, H. Pi, J. Yan, K. F. MacDonald, and X. Fang, "Coherently switching the focusing characteristics of all-dielectric metalenses," Opt Express **30**(15), 27683-27693 (2022).
5. F. He, K. F. MacDonald, and X. Fang, "Continuous beam steering by coherent light-by-light control of dielectric metasurface phase gradient," Opt Express **28**(20), 30107-30116 (2020).
6. Z. Li, M. H. Kim, C. Wang, Z. Han, S. Shrestha, A. C. Overvig, M. Lu, A. Stein, A. M. Agarwal, M. Loncar, and N. Yu, "Controlling propagation and coupling of waveguide modes using phase-gradient metasurfaces," Nat Nanotechnol **12**(7), 675-683 (2017).
7. R. Yang, Y. Shi, C. Dai, C. Wan, S. Wan, and Z. Li, "On-chip metalenses based on one-dimensional gradient trench in the broadband visible," Opt Lett **45**(20), 5640-5643 (2020).
8. L. Deng, Y. Xu, R. Jin, Z. Cai, and Y. Liu, "On-Demand Mode Conversion and Wavefront Shaping via On-Chip Metasurfaces," Adv. Opt. Mater. **10**(23), 2200910 (2022).
9. D. Ohana, B. Desiatov, N. Mazurski, and U. Levy, "Dielectric Metasurface as a Platform for Spatial Mode Conversion in Nanoscale Waveguides," Nano Lett **16**(12), 7956-7961 (2016).
10. A. Alquliah, M. Elkabbash, J. Cheng, G. Verma, C. S. Saraj, W. Li, and C. Guo, "Reconfigurable metasurface-based 1 × 2 waveguide switch," Photonics Res. **9**(10), 2104-2115 (2021).
11. A. He, X. Guo, T. Wang, and Y. Su, "Ultracompact Fiber-to-Chip Metamaterial Edge Coupler," ACS Photonics **8**(11), 3226-3233 (2021).
12. Y. Meng, Y. Chen, L. Lu, Y. Ding, A. Cusano, J. A. Fan, Q. Hu, K. Wang, Z. Xie, Z. Liu, Y. Yang, Q. Liu, M. Gong, Q. Xiao, S. Sun, M. Zhang, X. Yuan, and X. Ni, "Optical meta-waveguides for integrated photonics and beyond," Light Sci Appl **10**(1), 235 (2021).
13. Y. Shi, C. Wan, C. Dai, S. Wan, Y. Liu, C. Zhang, and Z. Li, "On-chip meta-optics for semi-transparent screen display in sync with AR projection," Optica **9**(6), 670-676 (2022).
14. H. Boo, Y. S. Lee, H. Yang, B. Matthews, T. G. Lee, and C. W. Wong, "Metasurface wavefront control for high-performance user-natural augmented reality waveguide glasses," Sci Rep **12**(1), 5832 (2022).
15. A. Yulaev, W. Zhu, C. Zhang, D. A. Westly, H. J. Lezec, A. Agrawal, and V. Aksyuk, "Metasurface-Integrated Photonic Platform for Versatile Free-Space Beam Projection with Polarization Control," ACS Photonics **6**(11), 2902-2909 (2019).
16. Z. Xie, T. Lei, F. Li, H. Qiu, Z. Zhang, H. Wang, C. Min, L. Du, Z. Li, and X. Yuan, "Ultra-broadband on-chip twisted light emitter for optical communications," Light Sci Appl **7**(4), 18001 (2018).
17. P. Genevet, D. Wintz, A. Ambrosio, A. She, R. Blanchard, and F. Capasso, "Controlled steering of Cherenkov surface plasmon wakes with a one-dimensional metamaterial," Nat Nanotechnol **10**(9), 804-809 (2015).
18. F. Ding, R. Deshpande, and S. I. Bozhevolnyi, "Bifunctional gap-plasmon metasurfaces for visible light: polarization-controlled unidirectional surface plasmon excitation and beam steering at normal incidence," Light Sci Appl **7**(4), 17178 (2018).
19. C. Chen, K. Kaj, X. Zhao, Y. Huang, R. D. Averitt, and X. Zhang, "On-demand terahertz surface wave generation with microelectromechanical-system-based metasurface," Optica **9**(1), 17-25 (2022).
20. J. Liu, X. Fang, F. He, S. Yin, W. Lyu, H. Geng, X. Deng, and X. Zheng, "Directional conversion of a THz propagating wave into surface waves in deformable metagratings," Opt Express **29**(14), 21749-21762 (2021).

21. Y. Zhang, Z. Li, W. Liu, Z. Li, H. Cheng, J. Tian, and S. Chen, "Multi-band on-chip photonic spin Hall effect and selective excitation of whispering gallery modes with metasurface-integrated microcavity," Opt Lett **46**(15), 3528-3531 (2021).
22. Y. Meng, Z. Liu, Z. Xie, R. Wang, T. Qi, F. Hu, H. Kim, Q. Xiao, X. Fu, Q. Wu, S.-H. Bae, M. Gong, and X. Yuan, "Versatile on-chip light coupling and (de)multiplexing from arbitrary polarizations to controlled waveguide modes using an integrated dielectric metasurface," Photonics Res. **8**(4), 564-576 (2020).
23. T. He, Y. Meng, Z. Liu, F. Hu, R. Wang, D. Li, P. Yan, Q. Liu, M. Gong, and Q. Xiao, "Guided mode meta-optics: metasurface-dressed waveguides for arbitrary mode couplers and on-chip OAM emitters with a configurable topological charge," Opt Express **29**(24), 39406-39418 (2021).
24. X. Guo, Y. Ding, X. Chen, Y. Duan, and X. Ni, "Molding free-space light with guided wave-driven metasurfaces," Sci Adv **6**(29), eabb4142 (2020).
25. C. Xie, L. Huang, W. Liu, W. Hong, J. Ding, W. Wu, and M. Guo, "Bifocal focusing and polarization demultiplexing by a guided wave-driven metasurface," Opt Express **29**(16), 25709-25719 (2021).
26. Y. Ding, X. Chen, Y. Duan, H. Huang, L. Zhang, S. Chang, X. Guo, and X. Ni, "Metasurface-Dressed Two-Dimensional on-Chip Waveguide for Free-Space Light Field Manipulation," ACS Photonics **9**(2), 398-404 (2022).
27. H. Xia, T. Sheng, J. Ding, M. Li, and Y. Yu, "High-efficiency one-dimensional metalens for 3D focusing," Opt Lett **47**(7), 1654-1657 (2022).
28. G.-B. Wu, S.-Y. Zhu, S. W. Pang, and C. H. Chan, "Superheterodyne-inspired waveguide-integrated metasurfaces for flexible free-space light manipulation," Nanophotonics **11**(20), 4499-4514 (2022).
29. Y. Ha, Y. Guo, M. Pu, X. Li, X. Ma, Z. Zhang, and X. Luo, "Monolithic-Integrated Multiplexed Devices Based on Metasurface-Driven Guided Waves," Adv. Theory Simul. **4**(2), 2000239 (2021).
30. B. Fang, Z. Wang, S. Gao, S. Zhu, and T. Li, "Manipulating guided wave radiation with integrated geometric metasurface," Nanophotonics **11**(9), 1923-1930 (2022).
31. Z. Huang, D. L. Marks, and D. R. Smith, "Out-of-plane computer-generated multicolor waveguide holography," Optica **6**(2), 119-214 (2019).
32. R. Yang, S. Wan, Y. Shi, Z. Wang, J. Tang, and Z. Li, "Immersive Tuning the Guided Waves for Multifunctional On-Chip Metaoptics," Laser Photonics Rev. **16**(8), 2200127 (2022).
33. P.-Y. Hsieh, S.-L. Fang, Y.-S. Lin, W.-H. Huang, J.-M. Shieh, P. Yu, and Y.-C. Chang, "Integrated metasurfaces on silicon photonics for emission shaping and holographic projection," Nanophotonics **11**(21), 4687-4695 (2022).
34. Y. Shi, C. Wan, C. Dai, Z. Wang, S. Wan, G. Zheng, S. Zhang, and Z. Li, "Augmented Reality Enabled by On-Chip Meta-Holography Multiplexing," Laser Photonics Rev. **16**(6), 2100638 (2022).
35. K. Xi, B. Fang, L. Ding, L. Li, S. Zhuang, and Q. Cheng, "Terahertz Airy beam generated by Pancharatnam-Berry phases in guided wave-driven metasurfaces," Opt Express **30**(10), 16699-16711 (2022).
36. E. D. Palik, *Handbook of Optical Constants of Solids* (Academic Press, 1998).
37. W. Lyu, J. M. Liu, S. Q. Yin, X. J. Deng, X. Fang, H. Geng, X. P. Zheng, "Deep-subwavelength gap modes in all-dielectric metasurfaces for high-efficiency and large-angle wavefront bending," Opt Express **30**(7), 12080-12091 (2022).
38. W. Song, R. Gatdula, S. Abbaslou, M. Lu, A. Stein, W. Y. Lai, J. Provine, R. F. Pease, D. N. Christodoulides, and W. Jiang, "High-density waveguide superlattices with low crosstalk," Nat Commun **6**(1), 7027 (2015).
39. B. Shen, R. Polson, and R. Menon, "Increasing the density of passive photonic-integrated circuits via nanophotonic cloaking," Nat Commun **7**(1), 13126 (2016).
40. S. Jahani, S. Kim, J. Atkinson, J. C. Wirth, F. Kalhor, A. A. Noman, W. D. Newman, P. Shekhar, K. Han, V. Van, R. G. DeCorby, L. Chrostowski, M. Qi, and Z. Jacob, "Controlling evanescent waves using silicon photonic all-dielectric metamaterials for dense integration," Nat Commun **9**(1), 1893 (2018).
41. J. Notaros, C. V. Poulton, M. J. Byrd, M. Raval, and M. R. Watts, "Integrated optical phased arrays for quasi-Bessel-beam generation," Opt Lett **42**(17), 3510-3513 (2017).
42. S. A. Miller, Y.-C. Chang, C. T. Phare, M. C. Shin, M. Zadka, S. P. Roberts, B. Stern, X. Ji, A. Mohanty, O. A. Jimenez Gordillo, U. D. Dave, and M. Lipson, "Large-scale optical phased array using a low-power multi-pass silicon photonic platform," Optica **7**(1), 3-6 (2020).
43. W. T. Chen, A. Y. Zhu, and F. Capasso, "Flat optics with dispersion-engineered metasurfaces," Nat. Rev. Mater. **5**(8), 604-620 (2020).
44. A. Vaskin, R. Kolkowski, A. F. Koenderink, and I. Staude, "Light-emitting metasurfaces," Nanophotonics **8**(7), 1151-1198 (2019).
45. S. Yin, F. He, W. Kubo, Q. Wang, J. Frame, N. G. Green, and X. Fang, "Coherently tunable metalens tweezers for optofluidic particle routing," Opt Express **28**(26), 38949-38959 (2020).
46. E. Shim, Y. Chen, S. Masmanidis, and M. Li, "Multisite silicon neural probes with integrated silicon nitride waveguides and gratings for optogenetic applications," Sci Rep **6**(1), 22693 (2016).
47. L. Li, Z. Liu, X. Ren, S. Wang, V.-C. Su, M.-K. Chen, C. H. Chu, H. Y. Kuo, B. Liu, W. Zang, G. Guo, L. Zhang, Z. Wang, S. Zhu, and D. P. Tsai, "Metalens-array-based high-dimensional and multiphoton quantum source," Science **368**(6498), 1487-1490 (2020).
48. C. W. Qiu, T. Zhang, G. Hu, and Y. Kivshar, "Quo Vadis, Metasurfaces?," Nano Lett **21**(13), 5461-5474 (2021).
49. K. J. Morton, G. Nieberg, S. Bai, and S. Y. Chou, "Wafer-scale patterning of sub-40 nm diameter and high aspect ratio (>50:1) silicon pillar arrays by nanoimprint and etching," Nanotechnology **19**(34), 345301 (2008).

50. Y. Meng, F. Hu, Z. Liu, P. Xie, Y. Shen, Q. Xiao, X. Fu, S.-H. Bae, and M. Gong, "Chip-integrated metasurface for versatile and multi-wavelength control of light couplings with independent phase and arbitrary polarization," Opt Express **27**(12), 16425-16439 (2019).